Superconductivity in the high-entropy alloy (NbTa)$_{0.67}$(MoHfW)$_{0.33}$

P. Sobota [1,2,*] R. Topolnicki [1,3] T. Ossowski [1] T. Pikula [4] A. Pikul [2] and R. Idczak [1]

[1]*Institute of Experimental Physics, University of Wrocław, Plac M. Borna 9, 50-204 Wrocław, Poland*
[2]*Institute of Low Temperature and Structure Research, Polish Academy of Sciences, Ulica Okólna 2, 50-422 Wrocław, Poland*
[3]*Dioscuri Center in Topological Data Analysis, Institute of Mathematics,*
Polish Academy of Sciences, Ulica Śniadeckich 8, 00-656 Warsaw, Poland
[4]*Institute of Electronics and Information Technology, Lublin University of Technology, Ulica Nadbystrzycka 38A, 20-618 Lublin, Poland*

Structural and physical properties of the high-entropy alloy (NbTa)$_{0.67}$(MoHfW)$_{0.33}$ were studied by x-ray powder diffraction, energy dispersive x-ray spectroscopy, magnetization, electrical resistivity, and specific heat measurements. The experimental results were supported by theoretical calculations using two complementary approaches for electronic structure calculations: the Korringa-Kohn-Rostoker method with the coherent potential approximation (KKR-CPA) and projector augmented wave (PAW) within the density functional theory. It was found that the alloy forms with a cubic, body-centered structure (space group $Im\bar{3}m$, W-type structure) with a lattice parameter $a = 3.287(1)$ Å and a random (but microscopically homogeneous) distribution of the constituent elements. At high temperature the alloy exhibits simple metallic behavior, while at low temperature it becomes a type-II superconductor with the critical temperature $T_c \approx 4.3$ K and the upper critical field $\mu_0 H_{c2} \approx 1.45$ T. The electron-phonon coupling constant calculated from the PAW data, $\lambda_{el-ph}^{th-PAW} = 0.63$, is in perfect agreement with the experimental results.

I. INTRODUCTION

High-entropy alloys (HEAs), i.e., solid solutions of five or more elements mixed in equimolar or near-equimolar ratios, have recently attracted much attention because of their unique and very promising physical properties. The most important feature that distinguishes HEAs from other alloys is that (contrary to the general understanding of physical metallurgy) they do not form multiple binary or ternary intermetallic compounds of the principal elements, but they form well-defined, simple, close-packed structures (body-centered cubic, face-centered cubic, or hexagonal). The name HEA comes from the large changes in configurational entropy during the formation of a solid solution from multiple elements with equimolar fractions, that were predicted by Yeh *et al.* [1].

The concept of HEA has opened up new possibilities in the engineering and design of functional materials. As a result, they have led to the discovery of HEAs with superior chemical, mechanical, and physical properties, such as strength comparable to that of metallic glasses and ceramics [2], high fracture toughness [3], corrosion resistance [4], and most recently, superconductivity [5]. According to Yeh [6], these intriguing properties can be mainly attributed to the following

basic effects: (i) Thermodynamic stabilization of the single phase with the high-entropy effect, (ii) retardation of the growth of the second phase from the single-phase solution due to slowed diffusion, (iii) excessive strength and slow kinetics due to strong lattice distortions, and finally (iv) the cocktail effect, in which the physical properties of HEA should be approximately the average of the properties of the elements in the composition.

From the point of view of solid state physics, one of the most interesting phenomena discovered in high-entropy alloys is superconductivity. The first HEA, in which this phenomenon was observed, was Ta$_{34}$Nb$_{33}$Hf$_8$Zr$_{14}$Ti$_{11}$, reported by Koželj *et al.* [5], which turned out to be a type-II superconductor with the critical temperature $T_c = 7.3$ K and the upper critical field $H_{c2} = 82$ kOe. It sparked a search that resulted in the discovery of more HEA superconductors based on transition metals, such as Hf$_{21}$Nb$_{25}$Ti$_{15}$V$_{15}$Zr$_{24}$ [7], Ta$_{1/6}$Nb$_{2/6}$Hf$_{1/6}$Zr$_{1/6}$Ti$_{1/6}$ [8], and Nb$_{10+2x}$Mo$_{35-x}$Ru$_{35-x}$Rh$_{10}$Pd$_{10}$ $(0 \leqslant x \leqslant 5)$ [9] (for a review, see also Ref. [10]). Moreover, the superconductivity was found not only in the HEA consisting of d-electron elements, but also in the alloy containing uranium, namely [TaNb]$_{0.31}$(TiUHf)$_{0.69}$ [11]. This extends the search for new HEA superconductors to alloys with actinides and possibly lanthanides.

Motivated by all those discoveries, we have undertaken a search for new HEA superconductors based on Ta and Nb, and mixed with other transition elements such as Ti, Zr, Hf, Mo, or W. In this paper, we report on the formation, crystal structure, and physical properties of a high-entropy alloy (NbTa)$_{0.67}$(MoHfW)$_{0.33}$.

---

*piotr.sobota3@uwr.edu.pl

II. EXPERIMENTAL AND COMPUTATIONAL DETAILS

A polycrystalline sample of $(NbTa)_{0.67}(MoHfW)_{0.33}$ was synthesized by conventional arc melting the stoichiometric amounts of elemental components (of at least 99.9% purity) in a Ti-gettered argon atmosphere. To avoid evaporation of the elements with the melting point much lower than that of tantalum, all the substrates were wrapped in Ta foil before melting, which was repeated several times to improve the homogeneity of the alloy. The total weight loss after synthesis was less than 0.2%.

The crystal structure of the so-obtained product was studied by powder x-ray diffraction (XRD) using a PANalytical X'pert Pro diffractometer with Cu $K\alpha$ radiation. The experimental XRD pattern was analyzed by the Rietveld method using the. HIGH SCORE PLUS software. The chemical composition and homogeneity of the sample were verified by energy dispersive x-ray spectroscopy (EDXS) using a FESEM FEI Nova NanoSEM 230 scanning electron microscope equipped with an EDAX Genesis XM4 spectrometer on a polished surface of the cut specimen.

The magnetic properties of the alloy were studied in the temperature range 1.72–300 K and in magnetic fields up to 20 kOe using a commercial Quantum Design magnetic properties measurement system (MPMS-XL) magnetometer. The heat capacity and electrical resistivity were measured from room temperature down to 1.8 K using a Quantum Design physical properties measurement system (PPMS) platform.

A high degree of chemical disorder is an inherent feature of HEA. In the case of the alloy $(NbTa)_{0.67}(MoHfW)_{0.33}$, as many as five different metal atoms randomly occupy lattice sites. A computational method commonly used to study the electron structure of such systems is the Korringa-Kohn-Rostoker formalism with the coherent potential approximation (KKR-CPA) [12–16]. In the present study, we used the KKR-CPA method implemented in the AkaiKKR (MACHIKANEYAMA) package [17–19]. The Perdew-Burke-Ernzerhof exchange-correlation functional (PBE) was applied to construct the muffin-tin crystal potential in the semirelativistic approach [20–22]. The cutoff for the angular momentum was set to $l_{max} = 3$ and 5216 k points were used to sample the irreducible part of the Brillouin zone during the self-consistent cycle and density of states (DOS) calculations. The muffin-tin radius was set to the largest nonoverlapping sphere, i.e., $R_{MT} = a\sqrt{3}/4$. The lattice parameter $a_{KKR-CPA} = 3.26$ Å, the bulk modulus $B_{KKR-CPA} = 194.5$ GPa, and its derivative $B'_{KKR-CPA} = 3.29$ of the crystal $(NbTa)_{0.67}(MoHfW)_{0.33}$ were derived using the third-order Birch-Murnaghan equation of state [23]. The results obtained by the KKR-CPA method were further verified by supercell density functional theory (DFT) calculations in the plane-wave function basis implemented in the Vienna *ab initio* simulation package (VASP) [24–26]. The electron exchange-correlation interactions were treated at the generalized gradient approximation (GGA) level using the PBE functional form. The electron ion-core interactions were represented by the projector augmented-wave (PAW) potentials [27,28]. A plane-wave basis set with a kinetic energy cutoff of 400 eV was applied. Since the supercell approach requires a well-defined position of all constituent species, three different
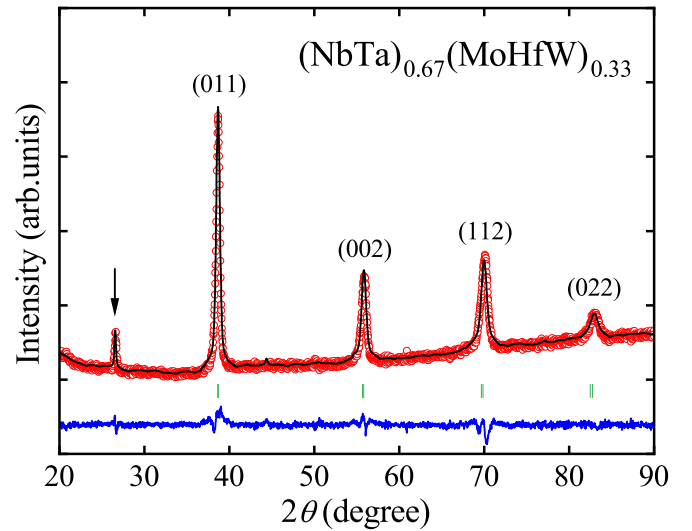

FIG. 1. Powder x-ray diffraction pattern of $(NbTa)_{0.67}(MoHfW)_{0.33}$ and results of its Rietveld refinement (see text for details). Red dots and the black line represent the experimental data and the theoretical curve, respectively. The blue line shows a difference between the two, and green dashes indicate positions of the Bragg reflections (also described by their corresponding Miller indices); an arrow indicates a reflection coming from a graphite sample holder.

random atomic arrangement were considered all containing 18 Ta and Nb atoms and 6 Mo, Hf, and W atoms to approximate the atomic composition of the studied HEA. The atoms were randomly placed at the nodes of the body-centered-cubic $3 \times 3 \times 3$ supercell. The lattice parameters derived using the third-order Birch-Murnaghan equation of state were for all three configurations close to $a_{PAW} = 3.29$ Å.

III. RESULTS AND DISCUSSION

A. Crystal structure and chemical composition

Figure 1 shows the powder XRD pattern obtained for the alloy $(NbTa)_{0.67}(MoHfW)_{0.33}$. The experimental data were easily indexed within a cubic, body-centered crystal structure (space group $Im\bar{3}m$, W-type structure). No reflections were detected from any secondary phases and the only additional peak visible at $2\theta = 26.6°$ was identified as the most intense reflection (002) from the graphite sample holder. In addition, no peaks were detected from any superstructure. Thus, it can be concluded that the synthesized alloy is a high-entropy alloy, i.e., all its constituent elements have been randomly incorporated into the crystal structure of the majority components (Ta and Nb), with no sign of any ordering in a lower symmetry structure. The values of the fitting parameters usually used to estimate the quality of the fit ($R_p = 2.5$, and $R_{wp} = 3.4$) demonstrate the good quality of the obtained results. The lattice parameter estimated by the Rietveld method for the solid solution studied, i.e., $a = 3.287(1)$ Å, is slightly smaller than that for pure Nb and Ta ($a = 3.303$ Å and $a = 3.306$ Å, respectively). This is most likely a consequence of the addition of two elements forming with much smaller bcc unit cells, i.e., molybdenum ($a \approx 3.147$ Å) and tungsten ($a \approx 3.165$ Å),
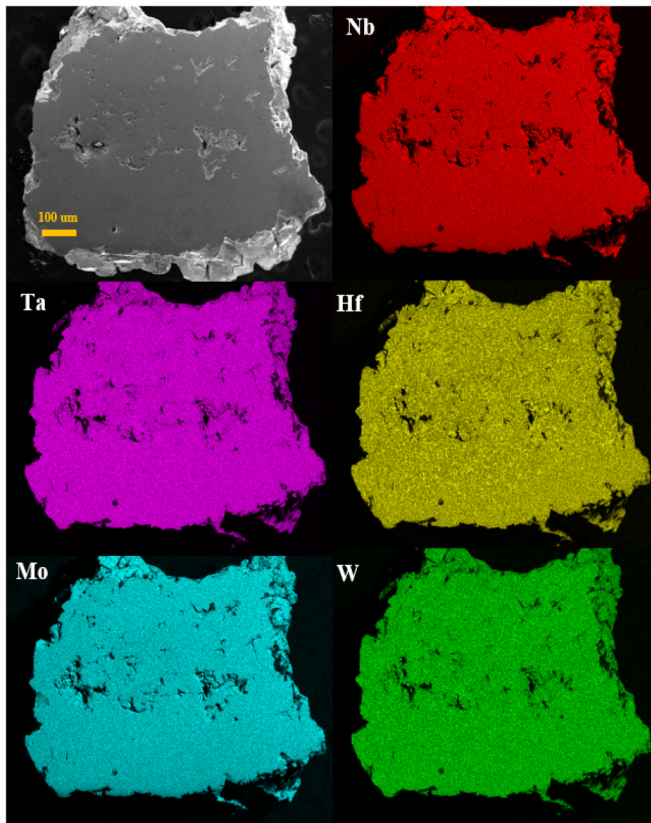
FIG. 2. SEM micrograph (top left image) and EDXS elemental mapping (other images) of the sample surface of $(NbTa)_{0.67}(MoHfW)_{0.33}$.

FIG. 3. (a) Temperature dependence of molar magnetic susceptibility χ_{mol} of $(NbTa)_{0.67}(MoHfW)_{0.33}$ in nominal applied magnetic field $\mu_0 H$, measured at low temperature in both zero-field-cooling (ZFC) and field-cooling (FC) regimes. (b) Field variation of mass magnetization σ of $(NbTa)_{0.67}(MoHfW)_{0.33}$ measured at various temperatures in the superconducting state; the inset displays $\sigma(H)$ in low fields and the straight solid line shows its linear-in-field part.

and only one forming with a significantly larger bcc unit cell, i.e., hafnium ($a \approx 3.615$ Å).

The EDXS analysis confirmed that, within the experimental accuracy, the composition of the synthesized alloy [i.e., 31.09(62) Nb–35.68(71) Ta–12.19(49) Mo–11.73(47) Hf–9.32(37) W at. %] is almost the same as the nominal one (i.e., 33.5 Nb– 33.5 Ta–11 Mo–11 Hf –11 W at. %). The small deviations are due to the limited accuracy of EDXS, the unevenness of the sample surface, and the overlapping of EDXS peaks in the emission spectra. The elemental mapping showed that the studied compound is a microscopically homogeneous mixture of the five constituent elements with no zones significantly enriched in any of the components (see Fig. 2). There is a possibility for minor phase segregation on the nanometer scale, as noted in other HEA superconductors, but its effect on the superconductive properties should be negligible as reported in Ref. [29].

B. Physical properties

Magnetic properties measurements revealed that over almost the entire temperature range studied, the alloy $(NbTa)_{0.67}(MoHfW)_{0.33}$ is a Pauli paramagnet with a very weak and nearly temperature-independent magnetic susceptibility of the order of 1.2×10^{-4} cm^3 mol^{-1} (not shown here). At low temperature, the susceptibility shows a clear transition to strong diamagnetism, which is characteristic of the superconducting state. As can be seen in Fig. 3(a), the
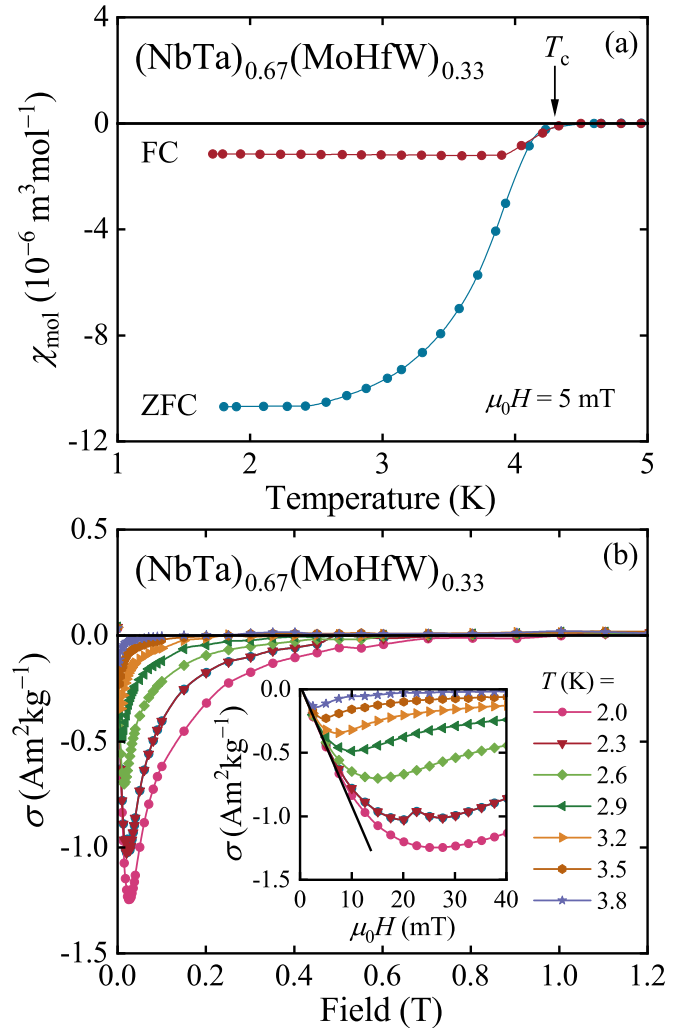
transition occurs at the critical temperature T_c of about 4.3 K. The large difference between the curves measured in the zero-field-cooling (ZFC) and field-cooling (FC) regimes indicates strong vortex pinning, characteristic of the type-II superconducting state and expected for HEA. Figure 3(b) shows field variations of the mass magnetization σ of the studied alloy, measured at various temperatures in the superconducting state. Taking the initial slope of the $\sigma(H)$ curve [see the inset to Fig. 3(b)] and assigning it to the fully developed Meissner state, we estimated the experimental demagnetization factor of the sample to be about 0.34. Using this value and the ZFC susceptibility/magnetization curves displayed in Fig. 3(a), we estimated the dimensionless volume susceptibility $4\pi\chi_V$ of the studied alloy as reaching about -0.73 at the lowest temperature studied, confirming the bulk and intrinsic character of the observed superconductivity. From the isotherms $\sigma(H)$ one can determine the values of the lower critical field $\mu_0 H_{c1}$,
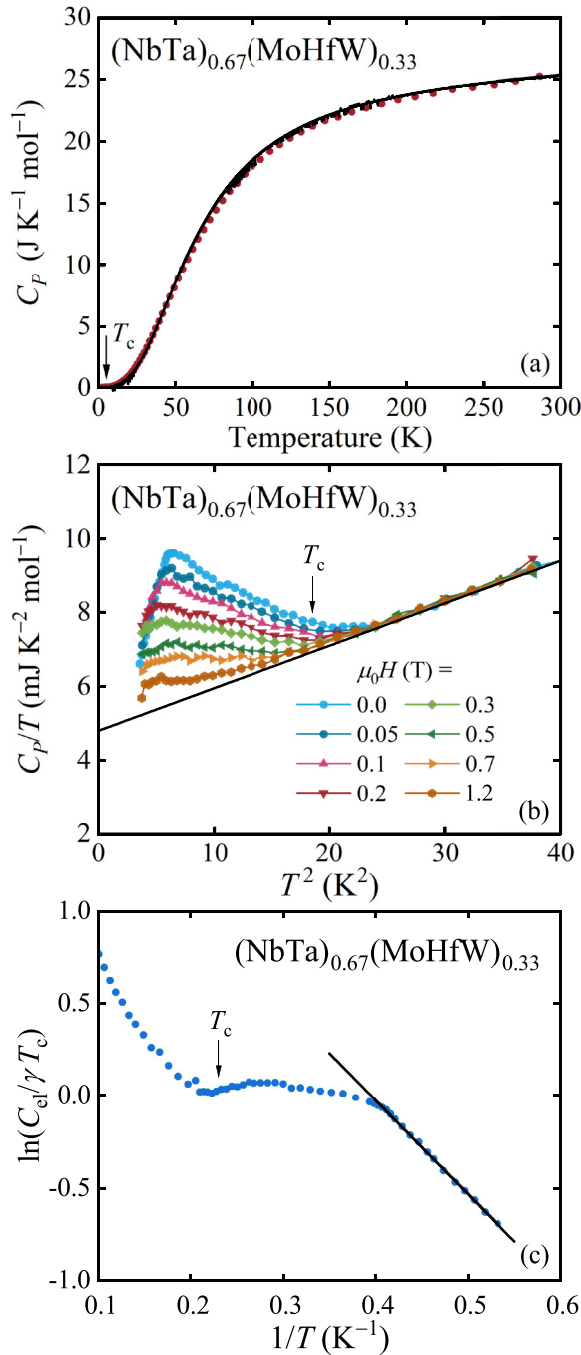
FIG. 4. (a) Temperature variation of specific heat C_P of $(NbTa)_{0.67}(MoHfW)_{0.33}$ (here displayed as C_P/T); the solid curve is a fit of Eq. (1) to the experimental data. (b) C_P/T vs. T^2 measured in various external magnetic fields $\mu_0 H$; the straight solid line is a fit to Eq. (2). (c) $\ln(C_{el}/\gamma T_c)$ as a function of inverse temperature, measured in zero magnetic field applied; the straight solid line is a fit of Eq. (8) to the experimental data.
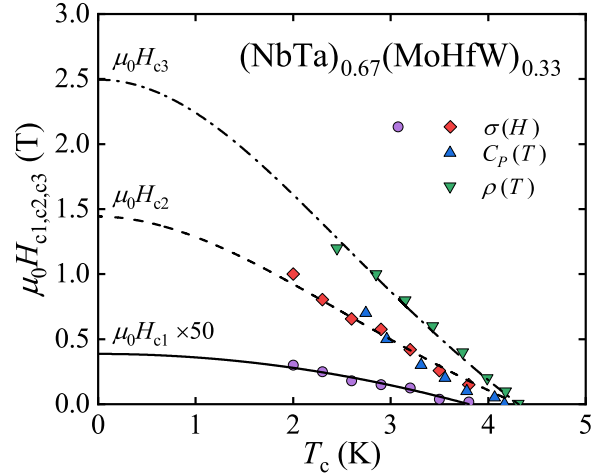

FIG. 5. Tentative phase diagram of superconducting $(NbTa)_{0.67}(MoHfW)_{0.33}$ determined from magnetization, specific heat, and resistivity measurements. Solid, dashed, and dashed-dotted lines are fits of Eq. (10) to the experimental curves $\mu_0 H_{c1}(T)$, $\mu_0 H_{c2}(T)$, and $\mu_0 H_{c3}(T)$, respectively.

and easily described by the conventional formula

$$C_P(T) = \gamma^{HT} T + 9Rr\left(\frac{T}{\Theta_D^{HT}}\right)^3 \int_0^{\Theta_D^{HT}/T} \frac{x^4 e^x}{(e^x-1)^2} dx, \quad (1)$$

where the first term is the conduction electron contribution to the specific heat according to the Sommerfeld model, and the second term represents the phonon contribution to $C_P(T)$ in terms of the Debye model, with the Sommerfeld coefficient γ^{HT} (the HT superscript indicates that coefficient was calculated from the entire range of the specific heat curve) and the characteristic Debye temperature Θ_D, as fitting parameters; R denotes the universal gas constant and r is the number of atoms in the formula unit [$r = 1$ for $(NbTa)_{0.67}(MoHfW)_{0.33}$]. Least-squares fits of Eq. (1) to the experimental data [see Fig. 4(a)] yielded the values $\gamma^{HT} = 4.4(7)$ mJ K^{-2} mol^{-1} and $\Theta_D^{HT} = 263(1)$ K. Figure 4(b) shows the low-temperature part of C_P/T of $(NbTa)_{0.67}(MoHfW)_{0.33}$ measured as a function of T^2 in various applied magnetic fields. As can be seen, in zero magnetic field the superconducting phase transition manifests itself as a distinct and quite broad λ-shaped-like anomaly that begins to be visible below about 4.3 K, which is consistent with T_c determined from the magnetic properties data. Although the origin of this broadening is uncertain, it may be due to the specific chemical composition of the studied alloy, as a similar effect has been observed in some HEA alloys regardless of their synthesis route or postprocessing [11,30]. Similar anomalies were also observed in superconductors with much simpler chemical compositions [31,32] that had some degree of phase inhomogeneity.

Such inhomogeneity could possibly result in a certain distribution of the T_c values, which could greatly complicate further analyses of the superconducting properties of our system, without bringing much new information about the type of superconductivity [see Supplemental Material [33] for data on the $C_P(T)$ phase transition described by assuming the distribution of T_c]. Therefore, in the rest of our paper we assumed a single T_c temperature in specific heat (i.e., 4.3 K), which

taking the points at which $\sigma(H)$ deviates from linearity [see the inset to Fig. 3(b)]. The resulting $\mu_0 H_{c1}(T)$ dependence is shown in Fig. 5.

The temperature dependence of the specific heat C_P of $(NbTa)_{0.67}(MoHfW)_{0.33}$ was found to be featureless above T_c

was determined from the inflection point of the zero-field C_P/T curve. Similarly, from the specific heat data measured in nonzero magnetic fields, the values of the upper critical field $\mu_0 H_{c2}$ can be determined by taking inflection points on the $C_P(T)/T$ curves. The resulting dependence $\mu_0 H_{c2}(T)$ is shown in Fig. 5 and described later in this paper.

Below about 6 K, C_P/T of $(NbTa)_{0.67}(MoHfW)_{0.33}$ can be described (in the normal state) by the T^3-Debye law [see Fig. 4(b)],

$$\frac{C_P(T)}{T} = \gamma^{LT} + \beta T^2, \tag{2}$$

with $\gamma^{LT} = 4.8(1)$ mJ K^{-2} mol^{-1} (where the LT superscript indicates that the coefficient was estimated using the low-temperature data) and $\beta = 0.115(1)$ mJ K^{-4} mol^{-1}, as fitting parameters, where

$$\beta = \frac{12}{5} r R \pi^4 \left(\frac{T}{\Theta_D^{LT}}\right)^3. \tag{3}$$

The characteristic Debye temperature Θ_D^{LT} estimated in this way is 256(1) K. Both γ^{LT} and Θ_D^{LT} are close to γ^{HT} and Θ_D^{HT} determined from the high-temperature fit displayed in Fig. 4(a), showing again the simple metallic behavior of the alloy in the normal state.

Together with T_c, the Θ_D^{LT} value thus estimated can be used to calculate the electron-phonon coupling constant λ_{el-ph} from the inverse McMillan's relation [34],

$$\lambda_{el-ph} = \frac{1.04 + \mu^* \ln\left(\frac{\Theta_D^{LT}}{1.45 T_c}\right)}{(1 - 0.62\mu^*)\ln\left(\frac{\Theta_D^{LT}}{1.45 T_c}\right) - 1.04}, \tag{4}$$

where μ^* is the Coulomb repulsion constant. Taking $\mu^* = 0.125$ (a value commonly accepted for d-electron elements), we obtained $\lambda_{el-ph} = 0.63(1)$, which allows us to classify the alloy $(NbTa)_{0.67}(MoHfW)_{0.33}$ as a superconductor with intermediate electron-phonon coupling. The strength of the coupling is definitely weaker compared to Zr-based superconducting high-entropy alloys [30].

Using γ^{LT}, one can estimate the experimental density of states of the conduction electrons at the Fermi level $N(E_F)$ from the formula

$$\gamma^{LT} = \tfrac{1}{3}\pi^2 k_B^2 N_A N(E_F) \tag{5}$$

as being of about 2.1(1) states eV^{-1} per formula unit (f.u.), which is a value comparable to that in the archetypal HEA superconductor [5]. The density of states of noninteracting electrons [35],

$$N(E_F)^* = \frac{N(E_F)}{1 + \lambda_{el-ph}}, \tag{6}$$

is then of about 1.3(1) states eV^{-1} f.u.$^{-1}$. And given the $N(E_F)$ value we can also estimate the Pauli susceptibility of the conduction electrons χ_P from the equation

$$\chi_P = \mu_B^2 N_A N(E_F) \tag{7}$$

as being of about $6.6(2) \times 10^{-4}$ cm^3 mol^{-1}, being consistent with the directly measured experimental (total) value of χ_{mol} (i.e., $\sim 1.2 \times 10^{-4}$ cm^3 mol^{-1}).

By subtracting the phonon contribution βT^3 estimated above [Eq. (2) and Fig. 4(b)] from the total specific heat C_P of $(NbTa)_{0.67}(MoHfW)_{0.33}$, one can estimate the electron contribution C_{el} to its specific heat. The resulting experimental dependence $C_{el}(T)$ [shown in Fig. 4(c) as $\ln(C_{el}/\gamma T_c)$ vs T^{-1}] can be easily described in the superconducting state in terms of the Bardeen-Cooper-Schrieffer (BCS) theory of superconductivity, i.e., by the formula [36]

$$C_{BCS}(T) = A\gamma^{LT} T_c \exp\left(-\frac{\Delta_0}{k_B T}\right), \tag{8}$$

where Δ_0 is a superconducting energy gap, and A is a constant. A least-squares fit of this formula to the experimental data [see the solid line in in Fig. 4(c)] gave $\Delta_0/k_B = 5.1(1)$ K, which leads to the normalized value $2\Delta_0/k_B T_c = 2.4(2)$.

The latter value is lower than the value of 3.52 predicted by the BCS theory (i.e., for a single, isotropic gap in the weak coupling limit), suggesting the occurrence of multigap superconductivity in $(NbTa)_{0.67}(MoHfW)_{0.33}$. However, since the quality of the fit in Fig. 4(c) is very good (and thus indicative of the single-gap superconductivity), the observed deviation of the parameter $2\Delta_0/k_B T_c$ from 3.52 is most likely due to the broadening of the transition at T_c caused by the crystallographic disorder inherently present in the HEA alloy studied, rather than to the multigap character of the superconductivity.

Taking the obtained values of the superconducting gap Δ_0/k_B and the Sommerfeld coefficient per volume $\gamma_V = 449.1$ J m^{-3} K^{-2} calculated from sample mass and density, the thermodynamic critical field $\mu_0 H_c(0)$ can be estimated according to the formula [37]

$$\mu_0 H_c(0) = \sqrt{\frac{3\gamma_V}{2\pi^2 \mu_0}} \frac{\Delta_0}{k_B}, \tag{9}$$

as equal to 13(1) mT in $(NbTa)_{0.67}(MoHfW)_{0.33}$.

The experimental curves $\mu_0 H_{c1}(T)$, $\mu_0 H_{c2}(T)$, and $\mu_0 H_{c3}(T)$ [the values of $\mu_0 H_{c3}(T)$ were derived from the resistivity data described later in the text] obtained for $(NbTa)_{0.67}(MoHfW)_{0.33}$ can be described by the Ginzburg-Landau equation

$$\mu_0 H_{ci}(T) = \mu_0 H_{ci}(0) \frac{1 - (T/T_c)^2}{1 + (T/T_c)^2} \tag{10}$$

(where $i = 1, 2, 3$), yielding $\mu_0 H_{c1}(0) = 7.7(1)$ mT, $\mu_0 H_{c2}(0) = 1.45(4)$ T, and $\mu_0 H_{c3}(0) = 2.49(5)$ T as least-squares fitting parameters (see the solid, dashed, and dashed-dotted lines, respectively, in Fig. 5). All the values are of the expected order of magnitude, and furthermore $\mu_0 H_{c2}(0)$ is close to the value of the orbital-limited upper critical field $\mu_0 H_{c2}^{orb}$ estimated from the formula developed for type-II superconductors in a dirty-limit scenario [38,39]:

$$\mu_0 H_{c2}^{orb} = -0.693 T_c \left[\frac{d(\mu_0 H_{c2}(T))}{dT}\right]_{T=T_c}. \tag{11}$$

Since $d[\mu_0 H_{c2}(T)]/dT|_{T=T_c}$ in $(NbTa)_{0.67}(MoHfW)_{0.33}$ is of about $-0.46(2)$ T K^{-1} (cf. Fig. 5), we get $\mu_0 H_{c2}^{orb} = 1.37(1)$ T. This value is in turn much smaller than the Pauli limiting field $\mu_0 H_P$, given by the relation [40]

$$\mu_0 H_P = 1.84 T_c, \tag{12}$$

which gives for the studied alloy a value of 7.9(2) T. In such a case, the Maki parameter [41]

$$\alpha_{\mathrm{M}} = \sqrt{2}\frac{\mu_0 H_{\mathrm{c2}}^{\mathrm{orb}}}{\mu_0 H_{\mathrm{P}}} \qquad (13)$$

is equal to 0.24(1), which indicates that the upper critical field is restricted in $(NbTa)_{0.67}(MoHfW)_{0.33}$ mainly by the orbital pair-breaking mechanism.

Using $\mu H_{\mathrm{c2}}(0)$ and $\mu_0 H_{\mathrm{c}}$ derived above one can also estimate the Ginzburg-Landau coherence length ξ_{GL} [42],

$$\xi_{\mathrm{GL}} = \frac{\phi_0}{2\pi \mu_0 H_{\mathrm{c2}}^{\mathrm{orb}}(0)}, \qquad (14)$$

and the Ginzburg-Landau penetration depth λ_{GL},

$$\lambda_{\mathrm{GL}} = \sqrt{\frac{\phi_0 \mu_0 H_{\mathrm{c2}}^{\mathrm{orb}}(0)}{4\pi \mu_0 H_{\mathrm{c}}(0)^2}}. \qquad (15)$$

The values obtained for $(NbTa)_{0.67}(MoHfW)_{0.33}$ are $\xi_{\mathrm{GL}} = 15.55(1)$ nm and $\lambda_{\mathrm{GL}} = 1125.1(9)$ nm, respectively. Taking these two values, the Ginzburg-Landau parameter κ_{GL}, defined as

$$\kappa_{\mathrm{GL}} = \frac{\lambda_{\mathrm{GL}}}{\xi_{\mathrm{GL}}}, \qquad (16)$$

can be calculated for the studied alloy as equal to 72.37(6), which indicates once more the type-II superconductivity.

To estimate the entropy associated with the superconducting state in the studied alloy, we used the experimental data $C_{\mathrm{el}}(T)$ [cf. Fig. 4(c)] and the formula

$$S_{\mathrm{sc}}(T) = \int_T^0 \frac{C_{\mathrm{el}}(T')}{T'}dT'. \qquad (17)$$

We also estimated the entropy associated with the normal state, assuming a linear contribution of electrons to the total specific heat [cf. Eq. (2)], i.e.,

$$S_{\mathrm{n}}(T) = \int_T^0 \frac{\gamma^{\mathrm{LT}}T'}{T'}dT' = \gamma^{\mathrm{LT}}T. \qquad (18)$$

We found that at the critical temperature T_{c}, S_{sc} of $(NbTa)_{0.67}(MoHfW)_{0.33}$ reaches a value of about 55 mJ K^{-1} mol^{-1}, which is more than twice the entropy in the normal state $S_{\mathrm{n}}(T_{\mathrm{c}}) = 23$ mJ K^{-1} mol^{-1}.

In a similar way, i.e., using the experimental data $C_{\mathrm{el}}(T)$ measured in zero magnetic field (for the superconducting state) and the linear term $\gamma^{\mathrm{LT}}T$ (for the normal state), the difference between the internal energy of the superconducting and normal states can be estimated as

$$\Delta U(T) = \int_T^0 [C_{\mathrm{el}}(T') - \gamma^{\mathrm{LT}}T']dT', \qquad (19)$$

while the difference between the entropy of these states can be calculated as

$$\Delta S(T) = \int_T^0 \frac{C_{\mathrm{el}}(T') - \gamma^{\mathrm{LT}}T'}{T'}dT'. \qquad (20)$$

With the $\Delta U(T)$ and $\Delta S(T)$ functions obtained in this way [see Fig. 6(a)], one can calculate the difference between the free energy of the superconducting and normal states,

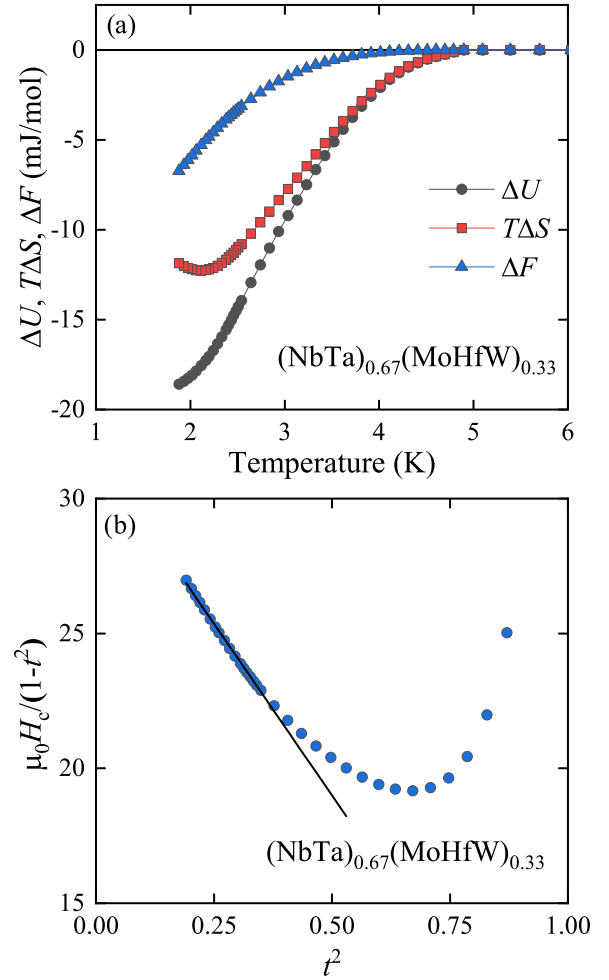$$\Delta F(T) = \Delta U(T) - T\Delta S(T), \qquad (21)$$

FIG. 6. (a) Differences between the internal energy ΔU, entropy multiplied by temperature $T\Delta S$, and free energy $\Delta F \propto -H_{\mathrm{c}}^2$ [see Eq. (22)], of the superconducting and normal states of $(NbTa)_{0.67}(MoHfW)_{0.33}$. (b) $\mu_0 H_{\mathrm{c}}/(1-t^2)$ vs t^2, where $t = T/T_{\mathrm{c}}$; the solid line is a fit of Eq. (23) to the experimental data.

which is also plotted in Fig. 6(a). Since

$$\Delta F(T) = -\frac{1}{2}V_{\mathrm{mol}}H_{\mathrm{c}}^2(T), \qquad (22)$$

(see, e.g., Ref. [43] and references therein), such a temperature variation of ΔF can be used to calculate the temperature variation of the thermodynamic critical field $H_{\mathrm{c}}(T)$. The so-derived experimental curve can be described at $T \rightarrow 0$ by the Taylor expansion [44]

$$\mu_0 H_{\mathrm{c}}(T) = \mu_0 H_{\mathrm{c}}(0)[1 - bt^2 - (1-b)t^4], \qquad (23)$$

where t is the normalized temperature ($t = T/T_{\mathrm{c}}$). A least-squares fit of Eq. (23) to the experimental data [shown in Fig. 6(b) as $-\mu_0 H_{\mathrm{c}}(T)/(1-t^2)$ vs t^2] gave the thermodynamic critical field $\mu_0 H_{\mathrm{c}}(0) = 32(1)$ mT, which is of the same order of magnitude as $\mu_0 H_{\mathrm{c}}(0)$ derived from Eq. (9) [i.e., 13(1) mT].

Figure 7(a) shows the temperature dependence of the electrical resistivity ρ of $(NbTa)_{0.67}(MoHfW)_{0.33}$ measured in zero applied magnetic field. As seen, at elevated temperatures the $\rho(T)$ curve is featureless and metallic in character, which is consistent with the results of magnetic susceptibility and
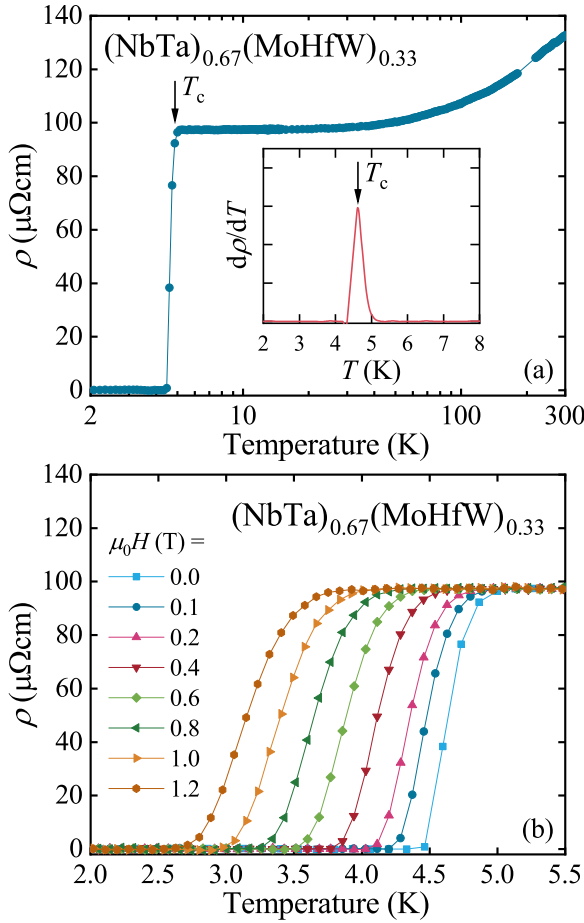
FIG. 7. (a) Electrical resistivity ρ of $(NbTa)_{0.67}(MoHfW)_{0.33}$ measured as a function of temperature in zero magnetic field; the inset shows the first derivative $d\rho/dT$ at low temperature. (b) $\rho(T)$ in various fields $\mu_0 H$. Arrows mark the critical temperature T_c and solid curves serve as guides for the eye.

specific heat measurements. The absolute values of ρ (varying from about 97 $\mu\Omega$ cm at 5 K to 132 $\mu\Omega$ cm at room temperature) are of the order of magnitude characteristic of intermetallic systems, and the rather small residual resistivity ratio RRR of about 1.4 (resulting mainly from high residual resistivity) is due to the polycrystalline nature of the sample and the high degree of structural disorder.

A sudden drop of the resistivity at low temperature manifests the superconducting transition with the critical temperature of about 4.6 K, which is slightly higher than $T_c =$ 4.3 K derived from the thermodynamic properties. As can be seen in Fig. 7(b), this transition shifts towards lower temperatures as the applied magnetic field increases, as in the other properties studied. However, the transition temperature (here defined as the highest temperature at which zero resistivity is observed) remains noticeably higher than the critical temperature derived from $C_P(T)$ (Fig. 4). Such a behavior indicates some contribution of the surface superconductivity in the studied alloy (which often occurs in bulk superconductors (see, e.g., Ref. [45]) and should be distinguished from the bulk superconductivity of $(NbTa)_{0.67}(MoHfW)_{0.33}$. Accordingly, we plotted the transition temperatures derived from $\rho(T)$ on

TABLE I. Experimentally determined basic characteristic parameters of normal and superconducting states in $(NbTa)_{0.67}(MoHfW)_{0.33}$ (for details, see the text).

Parameters	Values
T_c	4.3(1) K
γ^{HT}	4.4(7) mJ K^{-2} mol^{-1}
Θ_D^{HT}	263(1) K
γ^{LT}	4.8(1) mJ K^{-2} mol^{-1}
β	0.115(1) mJ K^{-4} mol^{-1}
Θ_D^{LT}	256(1) K
λ_{el-ph}	0.63(1)
$N(E_F)$	2.1(1) states eV^{-1} f.u.$^{-1}$
$N(E_F)^*$	1.3(1) states eV^{-1} f.u.$^{-1}$
χ_P	0.66(2)$\times 10^{-3}$ cm^3 mol^{-1}
$\mu_0 H_c(0)$	13.31(1) mT
$2\Delta_0/(k_B T_c)$	2.4(2)
$\mu_0 H_{c1}(0)$	7.77(1) mT
$\mu_0 H_{c2}(0)$	1.45(4) T
$\mu_0 H_{c3}(0)$	2.49(5) T
$[\frac{d(\mu_0 H_{c2}(T))}{dT}]_{T=T_c}$	$-0.46(2)$ T K^{-1}
$\mu_0 H_{c2}^{orb}$	1.37(1) T
$\mu_0 H_P$	7.1(2) T
α_M	0.24(1)
ξ_{GL} (nm)	15.55(1)
λ_{GL} (nm)	1125.1(9)
κ_{GL}	72.37(6)

the phase diagram in Fig. 5 as $\mu_0 H_{c3}(T)$, together with the curves $H_{c1}(T)$ and $H_{c2}(T)$ derived from the magnetization and specific heat measurements (mentioned above).

All the derived parameters describing the physical properties of $(TaNb)_{0.67}(MoHfW)_{0.33}$ are collected in Table I.

C. Theoretical results

The total and partial atomic densities of states of $(NbTa)_{0.67}(MoHfW)_{0.33}$ alloy calculated using the KKR-CPA method are shown in Fig. 8. The overall shape of total density of states (TDOS) is similar to those reported for the superconducting HEA $(NbTa)_{0.67}(HfZrTi)_{0.33}$ [46] and $Ta_{0.34}Nb_{0.33}Hf_{0.08}Zr_{0.14}Ti_{0.11}$ [47]. However, in the case of those two alloys, the Fermi level is located in the TDOS peak while in $(NbTa)_{0.67}(MoHfW)_{0.33}$ the Fermi level lies 0.44 eV above the nearest TDOS maximum. As can be seen, the largest contribution to TDOS in the Fermi-level region ($E - E_F$ from -6 to 2 eV) comes from Ta and Nb atoms, due to their highest atomic concentrations in the alloy. At the same time, partial atomic densities with angular momentum decomposition reveal that the main contributions to the TDOS are due to the d states of all constituent elements, i.e., $4d$ for Nb and Mo, and $5d$ for Ta, Hf, and W. The density of states at the Fermi level determined by the KKR-CPA method is 1.12 states eV^{-1} f.u.$^{-1}$. Inserting this value into relation (5), one can get the theoretical specific heat coefficient $\gamma_{th} = 2.64$ mJ K^{-2} mol^{-1}. In general, the DFT calculations (performed in this paper) take into account only the noninteracting electrons. Therefore the discrepancy between the theoretical γ_{th} and experimental value $\gamma^{LT} = 4.8$ mJ K^{-2} mol^{-1} allows us to
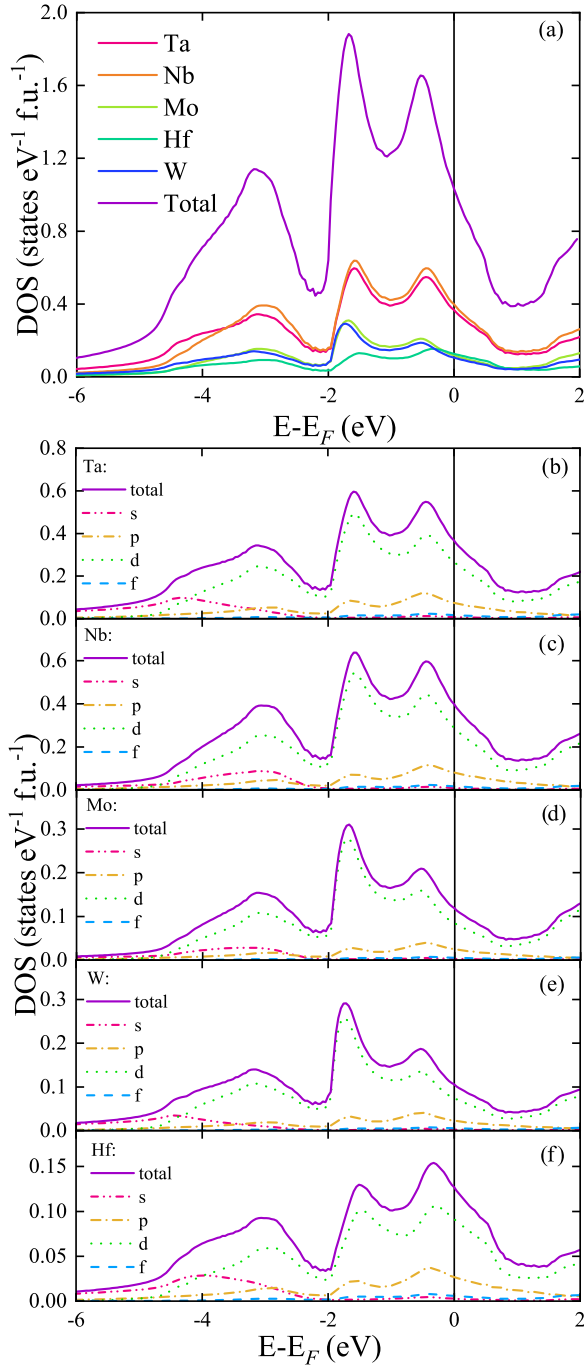
FIG. 8. Electron density of states of $(NbTa)_{0.67}(MoHfW)_{0.33}$ HEA calculated by the KKR-CPA method. (a) Total and partial atomic densities, color coded and weighted by their atomic concentrations. (b)–(f) Partial atomic densities with angular momentum decomposition.
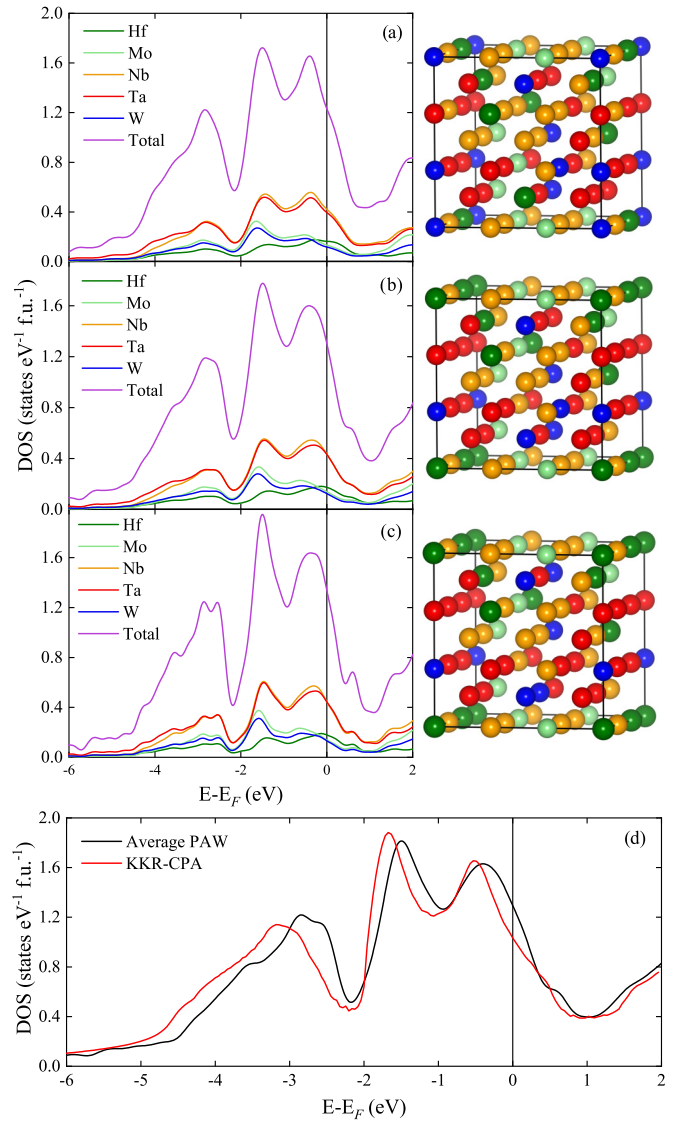

FIG. 9. (a)–(c) Total and partial atomic densities of states of $(NbTa)_{0.67}(MoHfW)_{0.33}$ calculated by the PAW method using VASP for three assumed random atomic arrangements which are shown in the right panel. (d) Averaged (over three configurations) TDOS with corresponding KKR-CPA data.

estimate the value of the electron-phonon coupling constant λ_{el-ph}^{th} by the equation [35,47]

$$\gamma^{LT} = \gamma_{th}\left(1 + \lambda_{el-ph}^{th}\right). \tag{24}$$

The calculated value of $\lambda_{el-ph}^{th-KKR} = 0.82$ from the KKR-CPA data is much higher than experimentally determined $\lambda_{el-ph} = 0.63$. By combining λ_{el-ph}^{th-KKR} with the experimental

value of Θ_D^{LT}, one can estimate T_c using McMillan's relation [Eq. (4)]. However, taking $\mu^* = 0.125$ leads to an overestimated $T_c = 8.8$ K. To explain this large discrepancy, two alternatives can be considered. The first one was proposed by Jasiewicz *et al.* [46,47] and assumes that the value of μ^* is much higher than 0.125. In the case of superconducting HEA $(NbTa)_{0.67}(HfZrTi)_{0.33}$, it was postulated that $\mu^* = 0.215$ [46]. Jasiewicz *et al.* argued that such high values of the Coulomb pseudopotential have been previously reported for various superconducting materials including Nb ($\mu^* = 0.21$) [48], V ($\mu^* = 0.3$) [48], Nb_3Ge ($\mu^* = 0.24$), [49] and $MgCNi_3$ ($\mu^* = 0.29$) [50]. If we accept that explanation then in order to correctly reproduce the experimental $T_c = 4.3$ K, $\mu^* = 0.206$ must be used. The second alternative is that the DOS obtained for HEA by the KKR-CPA method gives somewhat inaccurate results. Given this scenario, the results

obtained by the KKR-CPA method were further verified by supercell DFT calculations within the plane-wave function basis as implemented in the VASP.

Total and partial atomic densities of states of the $(NbTa)_{0.67}(MoHfW)_{0.33}$ alloy calculated by the PAW method using VASP are shown Figs. 9(a)–9(c). As can be seen, the results obtained for all three random atomic arrangements are very similar to each other. The averaged (over three configurations) TDOS is plotted in Fig. 9(d) together with corresponding KKR-CPA data. A closer look at this figure reveals that TDOS obtained by the KKR-CPA method is clearly shifted toward lower energy. The density of states at the Fermi level determined from the VASP data is 1.3 states eV^{-1} f.u.$^{-1}$. Using this value and applying the same procedure previously used for the KKR-CPA results, we got $\gamma_{th} = 2.94$ mJ K^{-2} mol^{-1} and $\lambda_{el-ph}^{th-PAW} = 0.63$. The latter value agrees perfectly with λ_{el-ph} determined from specific heat measurements using the McMillan's formula and the standard value of $\mu^* = 0.125$. Taking the above into account, it can be concluded that in the case of the studied superconducting HEA, DFT calculations by the PAW method give more reliable predictions than KKR-CPA. Moreover, it seems that the high value of the Coulomb pseudopotential ($\mu^* > 0.2$) postulated for $(NbTa)_{0.67}(HfZrTi)_{0.33}$ [46] is rather an artifact resulting from the KKR-CPA method.

IV. CONCLUSIONS

The formation and physical properties of a high-entropy alloy, namely $(TaNb)_{0.67}(MoHfW)_{0.33}$, are described. Refinement of the crystal structure showed that the alloy crystallizes in a simple bcc structure, as expected for HEA, and a microprobe analysis revealed a homogeneous distribution of elemental constituents in the studied sample. In turn, bulk physical properties measurements revealed that the alloy is a type-II superconductor with a critical temperature $T_c = 4.3(1)$ K and an upper critical field $\mu_0H_{c2}(0) = 1.45(4)$ T. An analysis of these properties indicates BCS-like superconductivity with intermediate electron-phonon coupling. Band structure calculations revealed that the PAW method gives more reliable predictions than KKR-CPA. In particular, the determined $\lambda_{el-ph}^{th-PAW} = 0.63$ is in excellent agreement with our experimental data, while $\lambda_{el-ph}^{th-KKR} = 0.82$.

[1] J.-W. Yeh, S.-K. Chen, S.-J. Lin, J.-Y. Gan, T.-S. Chin, T.-T. Shun, C.-H. Tsau, and S.-Y. Chang, Adv. Eng. Mater. **6**, 299 (2004).

[2] K. M. Youssef, A. J. Zaddach, C. Niu, D. L. Irving, and C. C. Koch, Mater. Res. Lett. **3**, 95 (2015).

[3] B. Gludovatz, A. Hohenwarter, D. Catoor, E. H. Chang, E. P. George, and R. O. Ritchie, Science **345**, 1153 (2014).

[4] Y. Chen, U. Hong, J. Yeh, and H. Shih, Scr. Mater. **54**, 1997 (2006).

[5] P. Koželj, S. Vrtnik, A. Jelen, S. Jazbec, Z. Jagličić, S. Maiti, M. Feuerbacher, W. Steurer, and J. Dolinšek, Phys. Rev. Lett. **113**, 107001 (2014).

[6] J.-W. Yeh, Eur. J. Control **31**, 633 (2006).

[7] N. Ishizu and J. Kitagawa, Results Phys. **13**, 102275 (2019).

[8] G. Kim, M.-H. Lee, J. H. Yun, P. Rawat, S.-G. Jung, W. Choi, T.-S. You, S. J. Kim, and J.-S. Rhyee, Acta Mater. **186**, 250 (2020).

[9] B. Liu, J. Wu, Y. Cui, Q. Zhu, G. Xiao, S. Wu, G. Cao, and Z. Ren, Scr. Mater. **182**, 109 (2020).

[10] L. Sun and R. J. Cava, Phys. Rev. Mater. **3**, 090301 (2019).

[11] W. Nelson, A. Chemey, M. Hertz, E. Choi, D. Graf, S. Latturner, T. Albrecht-Schmitt, K. Wei, and R. Baumbach, Sci. Rep. **10**, 4717 (2020).

[12] P. Soven, Phys. Rev. **156**, 809 (1967).

[13] G. D. Gaspari and B. L. Gyorffy, Phys. Rev. Lett. **28**, 801 (1972).

[14] W. H. Butler, Phys. Rev. B **31**, 3260 (1985).

[15] S. Kaprzyk and A. Bansil, Phys. Rev. B **42**, 7358 (1990).

[16] A. Bansil and S. Kaprzyk, Phys. Rev. B **43**, 10335 (1991).

[17] H. Akai, J. Phys. Soc. Jpn. **51**, 468 (1982).

[18] H. Akai, J. Phys.: Condens. Matter **1**, 8045 (1989).

[19] T. Kotani and H. Akai, Phys. Rev. B **54**, 16502 (1996).

[20] J. P. Perdew and Y. Wang, Phys. Rev. B **33**, 8800 (1986).

[21] J. P. Perdew, K. Burke, and M. Ernzerhof, Phys. Rev. Lett. **77**, 3865 (1996).

[22] J. P. Perdew, K. Burke, and Y. Wang, Phys. Rev. B **54**, 16533 (1996).

[23] F. Birch, Phys. Rev. **71**, 809 (1947).

[24] G. Kresse and J. Hafner, Phys. Rev. B **48**, 13115 (1993).

[25] G. Kresse and J. Furthmüller, Phys. Rev. B **54**, 11169 (1996).

[26] G. Kresse and J. Furthmüller, Comput. Mater. Sci. **6**, 15 (1996).

[27] P. E. Blöchl, Phys. Rev. B **50**, 17953 (1994).

[28] G. Kresse and D. Joubert, Phys. Rev. B **59**, 1758 (1999).

[29] S. Vrtnik, P. Koželj, A. Meden, S. Maiti, W. Steurer, M. Feuerbacher, and J. Dolinšek, J. Alloys Compd. **695**, 3530 (2017).

[30] F. von Rohr, M. J. Winiarski, J. Tao, T. Klimczuk, and R. J. Cava, Proc. Natl. Acad. Sci. USA **113**, E7144 (2016).

[31] A. Gabovich, M. S. Li, M. Pkaa, H. Szymczak, and A. Voitenko, Physica C **405**, 187 (2004).

[32] T. Liao, H. Sung, K. Syu, and W. Lee, Solid State Commun. **149**, 448 (2009).

[33] See Supplemental Material at http://link.aps.org/supplemental/10.1103/PhysRevB.106.184512 for detailed data on the $C_P(T)$ phase transition described assuming distribution of T_c.

[34] W. L. McMillan, Phys. Rev. **167**, 331 (1968).

[35] A. Tari, *The Specific Heat of Matter at Low Temperatures* (Imperial College Press/World Scientific, London, 2003).

[36] E. Gopal, *Specific Heats at Low Temperatures* (Springer, Berlin, 1966).

[37] R. D. Parks, *Superconductivity* (Taylor and Francis, London, 1969).

[38] E. Helfand and N. R. Werthamer, Phys. Rev. **147**, 288 (1966).

[39] N. R. Werthamer, E. Helfand, and P. C. Hohenberg, Phys. Rev. **147**, 295 (1966).

[40] A. M. Clogston, Phys. Rev. Lett. **9**, 266 (1962).

[41] K. Maki, Phys. Rev. **148**, 362 (1966).

[42] M. Tinkham, *Introduction to Superconductivity*, Dover Books on Physics Series (Dover, New York, 2004).

[43] M. Sahakyan and V. H. Tran, J. Phys.: Condens. Matter **28**, 205701 (2016).

[44] D. L. Decker, D. E. Mapother, and R. W. Shaw, Phys. Rev. **112**, 1888 (1958).

[45] D. Aoki, A. Huxley, E. Ressouche, D. Braithwaite, J. Flouquet, J.-P. Brison, E. Lhotel, and C. Paulsen, Nature (London) **413**, 613 (2001).

[46] K. Jasiewicz, B. Wiendlocha, K. Górnicka, K. Gofryk, M. Gazda, T. Klimczuk, and J. Tobola, Phys. Rev. B **100**, 184503 (2019).

[47] K. Jasiewicz, B. Wiendlocha, P. Korbe, S. Kaprzyk, and J. Tobola, Phys. Status Solidi RRL **10**, 415 (2016).

[48] S. Y. Savrasov and D. Y. Savrasov, Phys. Rev. B **54**, 16487 (1996).

[49] J. P. Carbotte, Rev. Mod. Phys. **62**, 1027 (1990).

[50] R. Szczęśniak, A. Durajski, and Ł. Herok, Solid State Commun. **203**, 63 (2015).